Dalton Transactions

ROYAL SOCIETY OF CHEMISTRY

PAPER

View Article Online
View Journal | View Issue

Cite this: *Dalton Trans.*, 2024, **53**, 10178

Synthesis and photoluminescence properties of high-quality reddish-orange emitting $Ca_4Nb_2O_9$:Eu^{3+} phosphors for WLEDs and anti-counterfeiting

Weiwei Xiang and Jae Su Yu *

In this report, we successfully synthesized a novel trivalent europium (Eu^{3+})-activated $Ca_4Nb_2O_9$ phosphor emitting reddish-orange light *via* its $^5D_0 \rightarrow {}^7F_1$ and $^5D_0 \rightarrow {}^7F_2$ transitions. In the $Ca_4Nb_2O_9$ host, Eu^{3+} ions exhibited optimal doping at a concentration of 15 mol%, with the concentration-quenching mechanism predominantly driven by electric dipole–dipole interactions. In addition, the $Ca_4Nb_2O_9$:Eu^{3+} phosphor exhibited excellent thermal stability with a photoluminescence (PL) intensity of 71.6% at a working temperature of 423 K. Interestingly, the internal PL quantum yield (PLQY) of the optimal sample was obtained to be 87.43%, and the external PLQY was determined to be 47.81%. The fabricated white light-emitting diode that employed this optimized phosphor alongside commercial phosphors, *via* a novel silica epoxy gel (parts A and B)-based method, exhibited good color rendering index (color rendering index = 80.65), excellent warm-correlated color temperature (correlated color temperature = 3753 K), and Commission International de l'Eclairage chromaticity coordinate (0.3922, 0.3845). Moreover, the optimal phosphor was introduced into the polyvinyl alcohol (PVA) polymer film, creating a translucent film. These films were then fabricated on glass, plastic, and card, which showed a satisfying emission under ultraviolet radiation. Consequently, the proposed Eu^{3+}-activated $Ca_4Nb_2O_9$ phosphors can be used as light sources and the $Ca_4Nb_2O_9$:Eu^{3+}-PVA film is proposed for anti-counterfeiting applications.

Received 5th April 2024,
Accepted 16th May 2024

DOI: 10.1039/d4dt01007h

rsc.li/dalton

1. Introduction

Recently, rare-earth ion doped inorganic compounds have garnered significant attention due to their excellent luminescence properties.[1,2] These properties have positioned them as key players in various applications such as lighting devices, biomarkers, medical instruments, optical thermometers, and anti-counterfeiting applications.[3–7] In particular, because of their high efficiency, long service time, and environmental-friendly features, white light-emitting diodes (WLEDs), which are a type of next-generation solid-state lighting source, have rapidly advanced lighting industry systems.[8,9] Moreover, solid-state combinations of different phosphors are commonly used to build phosphor-converted WLEDs (pc-WLEDs). The most commonly used commercial phosphors are YAG:Ce ($Y_3Al_5O_{12}$:Ce^{3+}), (Ba,Sr)$Si_2N_2O_2$:Eu^{2+}, β-Sialon:Eu^{2+} ($Si_{6-z}Al_zO_zN_{8-z}$, $0.1 \leq z \leq 2.0$), Sr_3SiO_5:Eu^{2+}, and KSF:Mn^{4+} (K_2SiF_6:Mn^{4+}).[10–14] Regrettably, conventional WLEDs employing yellow phosphors activated by blue InGaN LED chips possess spectral imperfections, which results in a high CCT value of approximately 7750 K and a CRI value of <80. These are in addition to the shortcomings of low luminous efficiency and an unstable spectrum.[15,16] To address these issues, research into red-green-blue phosphors co-activated LEDs has recently been conducted.[17,18] This approach offers the advantage of controlling the content of each component and adjusting the performance of the triangular LED system accordingly.

Trivalent europium (Eu^{3+}) is a typical activating ion in red-emitting materials. In response to its charge transfer band (CTB) and featured transitions ($^7F_0 \rightarrow {}^5D_4$, ^5G_J, $^5L_6$, and $^5D_3$) occurring between 200–300 nm and 300–450 nm, it expresses good absorption capabilities in the ultraviolet (UV) and near-UV (NUV)[19,20] ranges. The emission characteristics of Eu^{3+} are sensitive to symmetry, affecting the performance of both the electric dipole (ED) and magnetic dipole (MD) transitions. When inversion symmetry is dominant, the Eu^{3+} ions emit approximately 591 nm emission for the MD transition ($^5D_0 \rightarrow {}^7F_1$), while the ED transition ($^5D_0 \rightarrow {}^7F_2$) is forbidden. In contrast, in a non-inversion symmetric crystal environment, the main spectrum in emission is governed by the ED transition, resulting in radiation of approximately 613 nm.[21,22] In this case, selecting an ideal host lattice is essential for enhancing the emission efficiency.

Department of Electronic and Information Convergence Engineering, Institute for Wearable Convergence Electronics, Kyung Hee University, Yongin-si, Gyeonggi-do 17104, Republic of Korea. E-mail: jsyu@khu.ac.kr

Owing to their outstanding crystal diversity and multifunctionality, niobates serve as significant host materials that have attracted considerable interest in indoor lighting devices, meeting the requirements of industrial products. Some new niobate-based phosphors such as $Sr_3CaNb_2O_9:Eu^{3+}$, $Ca_2InNbO_6:Sm^{3+}$, $Na_2Ca_2Nb_4O_{13}:Eu^{3+}$, $Li_6CaLa_2Nb_2O_{12}:Yb/Er$, $LaMg_{0.402}Nb_{0.598}O_3:Pr^{3+}$, and $Ba_3ZnNb_2O_9:Eu^{3+}$ have been reported.[23–28] Zhang *et al.* suggested that $Ca_4Nb_2O_9:Pr^{3+}$ phosphors could compensate for the flickering behavior of alternating current (AC)-LEDs and might be suitable for application in AC-LEDs.[29] However, to the best of our knowledge, there is no reported study on $Ca_4Nb_2O_9:Eu^{3+}$ phosphors.

In addition, the application of rare-earth phosphors in anti-counterfeiting measures is widespread in the era of information security. Compared to the existing anti-counterfeiting technologies, rare-earth-activated phosphors have significant advantages in terms of cost, convenience, safety, transparency, convenient inspection, defensiveness, and efficiency.[30,31] These advantages render phosphor-based confidentiality methods competitive.

In this study, Eu^{3+} doped $Ca_4Nb_2O_9$ phosphors with different dopant concentrations were synthesized through a high-temperature solid-state reaction. The properties of the synthesized phosphors were analyzed, including their PL excitation (PLE) and PL emission spectra, Commission International de l'Eclairage (CIE) chromaticity coordinates, and color purity. Additionally, the concentration quenching, thermal quenching, and decay lifetimes of these materials were investigated. Finally, red-emitting LED and WLED devices using the developed phosphors were packaged *via* a novel method for practical applications. The as-prepared phosphors were introduced in security applications.

2. Experimental procedure

The raw materials used for the synthesis of the $Ca_4Nb_2O_9:Eu^{3+}$ phosphors included calcium carbonate ($CaCO_3$, 99.99%), niobium(v) oxide (Nb_2O_5, 99.99%), and europium(III) oxide (Eu_2O_3, 99.99%), which were purchased from Sigma-Aldrich without further purification. Through a high-temperature solid-state reaction technique, a series of $Ca_4Nb_2O_9:xEu^{3+}$ (x = 0.01–0.25) phosphors were synthesized. After being weighed and ground, the mixture was transferred into alumina crucibles, being heated at 1350 °C for 12 h. Finally, the samples were cooled down to room temperature and ground for 30 min.

Red-emitting LED and WLED devices were fabricated using silica epoxy gel (parts A and B), the optimized $Ca_4Nb_2O_9:Eu^{3+}$ phosphor, and commercial blue and green phosphors. For the red-emitting LED device, 0.1 g of $Ca_4Nb_2O_9:0.15Eu^{3+}$ phosphor was mixed with 0.5 g of silica epoxy gel, and for the WLED device, 0.1 g of $Ca_4Nb_2O_9:0.15Eu^{3+}$ phosphor, 0.05 g of $BaMgAl_{10}O_{17}:Eu^{2+}$ blue phosphor (BAM:Eu^{2+}), and 0.07 g of $BaSc_2Si_3O_{10}:Eu^{2+}$ green phosphor (BSS:Eu^{2+}) were mixed with 1 g of silica epoxy gel. The as-prepared slurries were applied onto the 405 nm emitting chips and dried in an oven at 80 °C for 6 h.

The flexible luminescent anti-counterfeit films were synthesized by mixing the phosphor with a polyvinyl alcohol (PVA) solution. First, the PVA powder was diffused in pure water at a 15% weight ratio and stirred at 90 °C for 1 h. After the mixture formed a transparent solution, heating was stopped, and the phosphor was added. Following stirring for another 1 h, the mixture was smeared onto glass and plastic bases.

A diffractometer (Bruker D8 Advance, utilizing Cu Kα radiation (λ = 0.154056 nm)) was employed to investigate the crystalline structures of as-prepared samples with X-ray diffraction (XRD) within the 2θ range of 5°–90°. Their morphologies were analyzed by field-emission scanning electron microscopy (FE-SEM; Carl Zeiss). Energy-dispersive X-ray spectroscopy (EDS) elemental mapping images were measured using an instrument attached to the FE-SEM. The PLE and PL emission spectra of the prepared samples were obtained by using a fluorescence spectrophotometer (Scinco Fluorometer FS-2). For the optimized sample, X-ray photoelectron spectroscopy (XPS, K-alpha (Thermo Electron)) analysis was conducted.

3. Results and discussion

To identify the phases of the as-synthesized phosphor samples, XRD analysis was carried out, as displayed in Fig. 1. The XRD pattern of undoped $Ca_4Nb_2O_9$ closely matched that of PDF card 49-0910, and little difference was observed when Eu^{3+} ions were introduced into the host lattice, which suggests that the Eu^{3+} ions caused a slight change in the crystal structure when introduced into the host lattice. The radius deviation (D_r) between the doped and host ions was calculated using the following equation:[32]

$$D_r = \frac{R_s - R_d}{R_s} \times 100\% \quad (1)$$

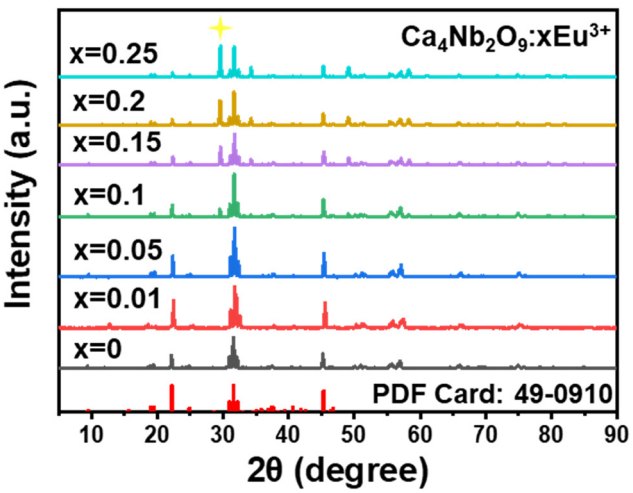

Fig. 1 XRD patterns of the prepared $Ca_4Nb_2O_9:xEu^{3+}$ (x = 0, 0.01, 0.05, 0.1, 0.15, 0.2, and 0.25, in mol) phosphors.

where R_s and R_d are the effective ionic radii of the host and dopant ions, respectively. In this study, the dopant ion used was Eu^{3+} (CN = 6, $R_{Eu^{3+}}$ = 0.95 Å), and the coordination number (CN) of Ca^{2+} ions is either 6 (CN = 6, $R_{Ca^{3+}}$ = 1.00 Å) or 7 (CN = 7, $R_{Ca^{3+}}$ = 1.06 Å).[33,34] To ensure that the doped crystal can be obtained, D_r should be below 30%, with D_r values of Eu^{3+}–Ca^{2+} calculated to be 5% and 10.37% for the coordination numbers of 6 and 7, respectively. However, the impurity peak at approximately 29.6° increased as the dopant concentration increased, which is attributed to the impurity phase of $EuNb_4O_{11}$ (PDF card: 33-0546), as indicated in Fig. 1 with a star. In the $Ca_4Nb_2O_9$ phosphor, when Eu^{3+} ions occupy the sites of Ca^{2+} ions, maintaining valence balance becomes challenging. In such cases, the extra positive charges result in the repulsion that prevents further substitution.[35]

To investigate the elemental composition and chemical states of atoms in the $Ca_4Nb_2O_9$:Eu^{3+} phosphor, XPS analysis was performed in the energy range of 0–1400 eV and the spectrum is shown in Fig. 2(a). Peaks for all the elements (Ca, Nb, O, and Eu) and additional carbon were observed. The C 1s peak at 284.8 eV served as the calibration reference. Peaks for Ca, Nb, O, and Eu were observed in the XPS survey scan spectrum. The high-resolution XPS (HR-XPS) spectra of each element are illustrated in Fig. 2(b–e). The two peaks located at 346.53 and 350.07 eV correspond to Ca $2p_{1/2}$ and $2p_{3/2}$, respectively,[36] while the peaks at the binding energies of 206.70 and 209.45 eV are associated with Nb $3d_{3/2}$ and $3d_{5/2}$, respectively.[37] In the O 1s core-level spectrum, the broad peak represents a combination of three peaks (529.58, 531.34, and 533.41 eV),[38] which are ascribed to lattice oxygen, oxygen vacancies, and

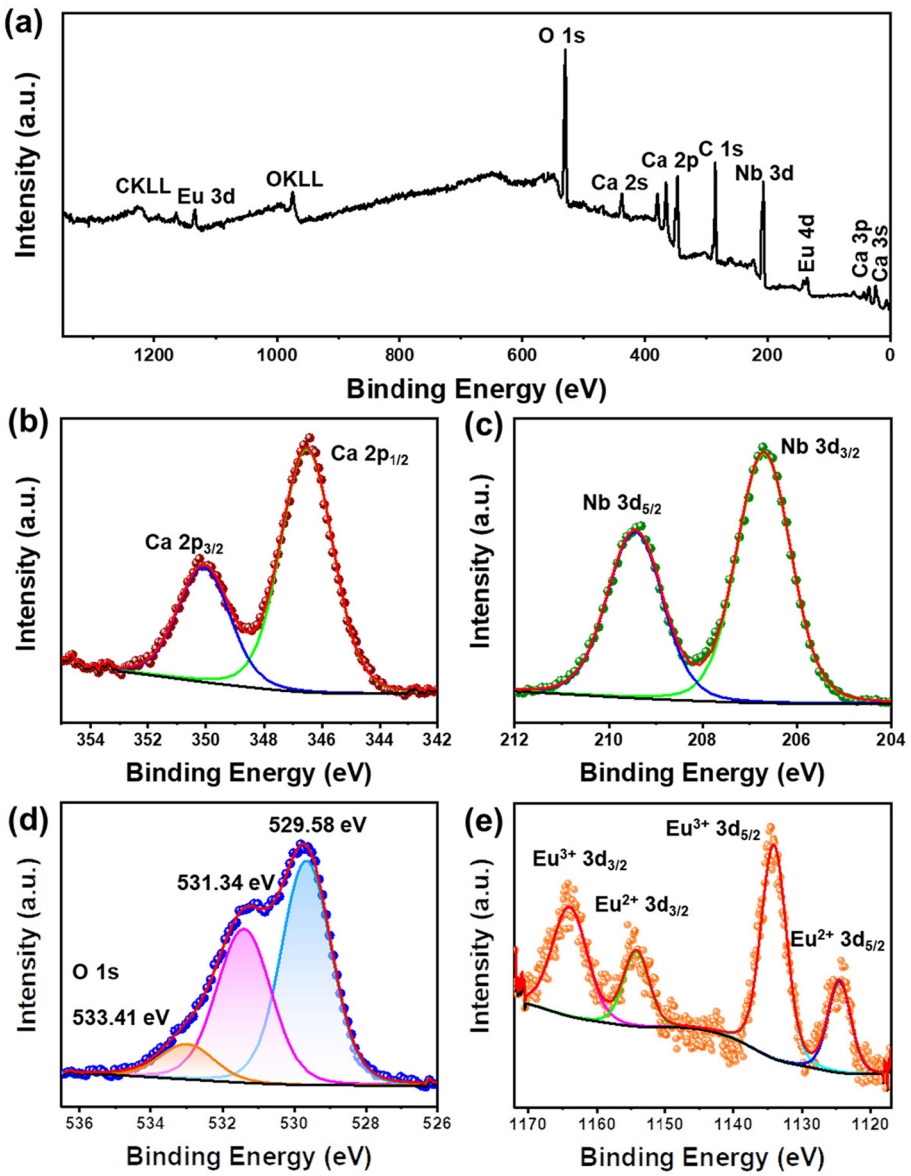

Fig. 2 (a) Total XPS survey scan spectrum of the $Ca_4Nb_2O_9$:0.15Eu^{3+} phosphor. (b–e) HR-XPS core-level spectra of Ca 2p, Nb 3d, O 1s, and Eu 3d.

surface oxygen, respectively. The HR-XPS spectrum of Eu 3d revealed four peaks at 1163.99, 1154.29, 1134.12, and 1124.56 eV, which belong to Eu^{3+} $3d_{3/2}$, Eu^{2+} $3d_{3/2}$, Eu^{3+} $3d_{5/2}$, and Eu^{2+} $3d_{5/2}$, respectively.[39] The appearance of the Eu^{2+} 3d peaks suggests the presence of two Eu ion environments.

The FE-SEM images of the optimal sample $Ca_4Nb_2O_9$:0.15Eu^{3+} with various scales are presented in Fig. 3(a–d), indicating the non-uniform microstructure of the $Ca_4Nb_2O_9$ phosphor. This is a common phenomenon observed in materials synthesized *via* high-temperature solid-state methods, which exhibited irregular shapes and agglomerations. The elemental mapping images are compared in Fig. 3(e), demonstrating the homogenous distribution of Ca, Nb, O, and Eu within the compound. The peaks corresponding to Ca, Nb, O, and Eu elements are illustrated in the EDS spectrum (Fig. 3(f)).

To investigate the band gaps of the host and optimal samples, the diffuse reflection spectroscopy (DRS) spectra are compared in Fig. 4(a). The Eu^{3+}-doped phosphor exhibited absorption peaks at 300, 395, 466, and 527 nm. The band gaps of both the host and doped phosphor samples were estimated using the Kubelka–Munk (K–M) function:[40]

$$F(R_\infty) = \frac{(1-R)^2}{2R} = \frac{K}{S} \quad (2)$$

where R, K, and S are the reflectance, absorption, and scattering coefficients, respectively. As $F(R_\infty)$ is directly proportional to K, when the Tauc equation given as eqn (3) is introduced, the relationship between $F(R_\infty)$ and energy gap (E_g) can be investigated:[41]

$$(\alpha h\nu)^n = A(h\nu - E_g) \quad (3)$$

$$(F(R_\infty)h\nu)^n = A(h\nu - E_g) \quad (4)$$

where $h\nu$ represents the photon energy, A stands for a constant, and n is a transition type-related constant. When transitions are directly authorized, indirectly allowed, directly prohibited, or indirectly forbidden, the n values are 1/2, 2, 3/2, and 3, respectively. For the $Ca_4Nb_2O_9$, n is 2.[29] The relationship

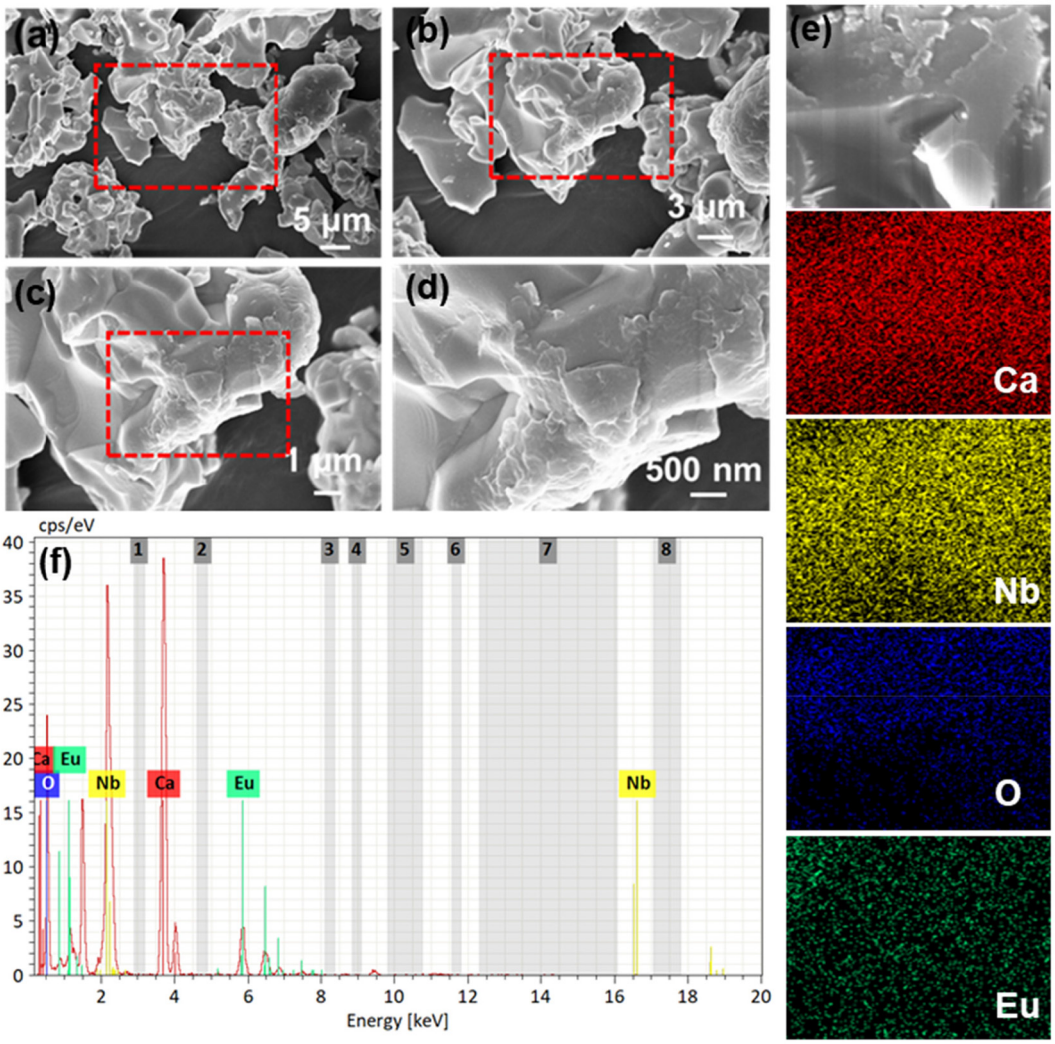

Fig. 3 (a–d) FE-SEM images of the $Ca_4Nb_2O_9$:0.15Eu^{3+} phosphor at different magnifications. (e) Elemental mapping images and (f) EDS spectrum of the as-synthesized phosphor.

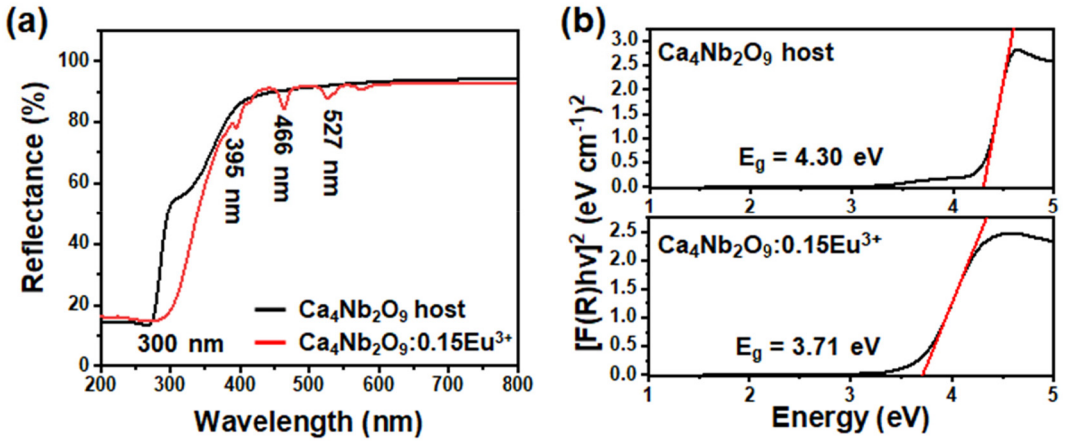

Fig. 4 (a) DRS spectra and (b) Tauc plots of $Ca_4Nb_2O_9$ host and $Ca_4Nb_2O_9$:0.15Eu^{3+} phosphor.

between $(F(R_\infty)h\nu)^2$ and $h\nu$ is obtained in Fig. 4(b). The E_g values were determined by the extrapolation of the tangent drawn in this figure to zero, resulting in 4.30 and 3.71 eV. The significant decrease in the E_g value is primarily attributed to the shrinking of the optical bandgap resulting from the doping of Eu^{3+} ions, which endowed the Eu^{3+}-doped $Ca_4Nb_2O_9$ phosphors with improved luminescence properties.[42]

Fig. 5(a) shows the comparative PLE spectra at an emission wavelength of 615 nm for the $Ca_4Nb_2O_9$:$x$$Eu^{3+}$ (where x ranges from 0.01 to 0.25) phosphors. The wide peak at approximately

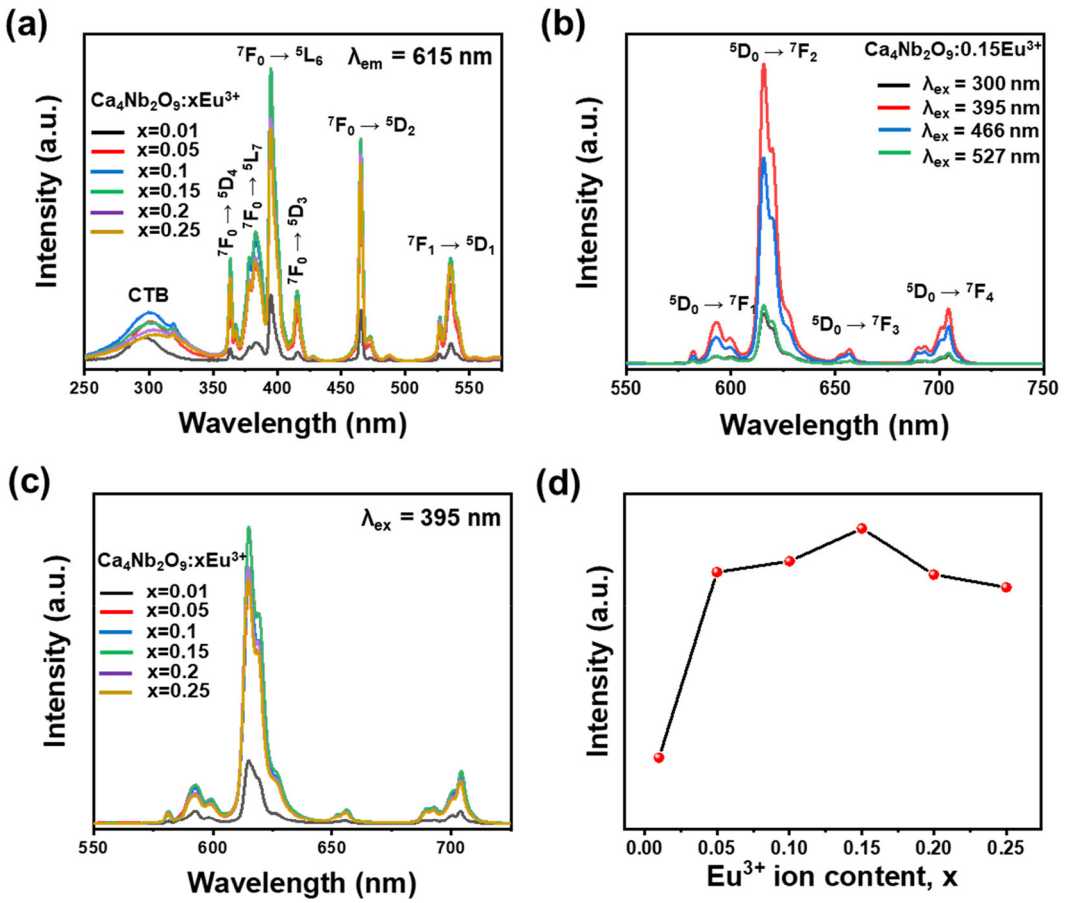

Fig. 5 (a) PLE spectra of $Ca_4Nb_2O_9$:$x$$Eu^{3+}$ (x = 0.01, 0.05, 0.1, 0.15, 0.2, and 0.25, in mol) phosphors, monitored at 615 nm, (b) PL emission spectra of the $Ca_4Nb_2O_9$:0.15Eu^{3+} phosphor excited at 300, 395, 466, and 527 nm, and (c) PL emission spectra of the $Ca_4Nb_2O_9$:$x$$Eu^{3+}$ phosphors excited at 395 nm. (d) Normalized emission intensity for different Eu^{3+} ion concentrations.

300 nm is attributed to the CTB of O^{2-}–Eu^{3+}. A series of absorption peaks from 350 to 550 nm for the f–f transition were observed, with the peaks located at 364, 384, 395, 406, 466, and 527 nm (similar to the absorption peaks shown in Fig. 4(a)) corresponding to the $^7F_0 \rightarrow {}^5D_4$, $^7F_0 \rightarrow {}^5L_7$, $^7F_0 \rightarrow {}^5L_6$, $^7F_0 \rightarrow {}^5D_3$, $^7F_0 \rightarrow {}^5D_2$, and $^7F_1 \rightarrow {}^5D_1$ transitions.[43,44] Fig. 5(b) shows the emission spectra of the optimal phosphor with the excitation wavelengths of 300, 395, 466, and 527 nm. With the highest PL intensity, 395 nm was considered the ideal excitation wavelength for the as-prepared samples. Fig. 5(c) shows the PL emission spectra of Eu^{3+} doped phosphors with different dopant concentrations. The emission peaks at 588, 615, 655, and 712 nm are ascribed to the transitions from $^5D_0$ to ^7F_J (where J = 1, 2, 3, and 4), respectively.[45] The results of the luminescence measurements revealed that as the Eu^{3+} ion concentration increased, there was practically no change in the shapes and positions of these peaks. As shown in Fig. 5(d), the PL intensity initially increased and then decreased as the Eu^{3+} ion concentration increased, reaching a peak at 15 mol%, which could be attributed to concentration quenching. The critical distance (R_c) can be determined based on Blasse's model:[46]

$$R_c = 2\left(\frac{3V}{4\pi x_c Z}\right)^{\frac{1}{3}} \quad (5)$$

where V, X_c, and Z denote the volume, critical concentration, and cation number, respectively. For the $Ca_4Nb_2O_9$ phosphor, the values were 767.048 Å^3, 0.15, and 4. From this, the R_c value was obtained as 13.47 Å, which was much greater than 5 Å, indicating that the concentration quenching is dependent on multipole interactions. In addition, several types of multipole interactions occur in concentration quenching: dipole–dipole (d–d), dipole–quadrupole (d–q), and quadrupole–quadrupole (q–q).[47] To determine the key interactions, an equation including the interaction constant Q is expressed as follows:[48]

$$\frac{I}{x} = k\left(1 + \beta(x)^{\frac{Q}{3}}\right)^{-1} \quad (6)$$

where I and x represent the intensity and dopant-ion concentration, respectively. If Q is equal to 6, 8, and 10, the main interactions are electric d–d, d–q, and q–q interactions. For easier investigation, the equation can be rewritten as follows:[49]

$$\log\left(\frac{I}{x}\right) = C - (Q/3)\log(x) \quad (7)$$

As shown in Fig. 6(a), the slope was −1.43, representing that Q was 4.29, approaching 6. This suggests that the electric d–d interaction enables non-radiative (NR) energy transfer of the dopant ions in the compound. The ratios of MD transition

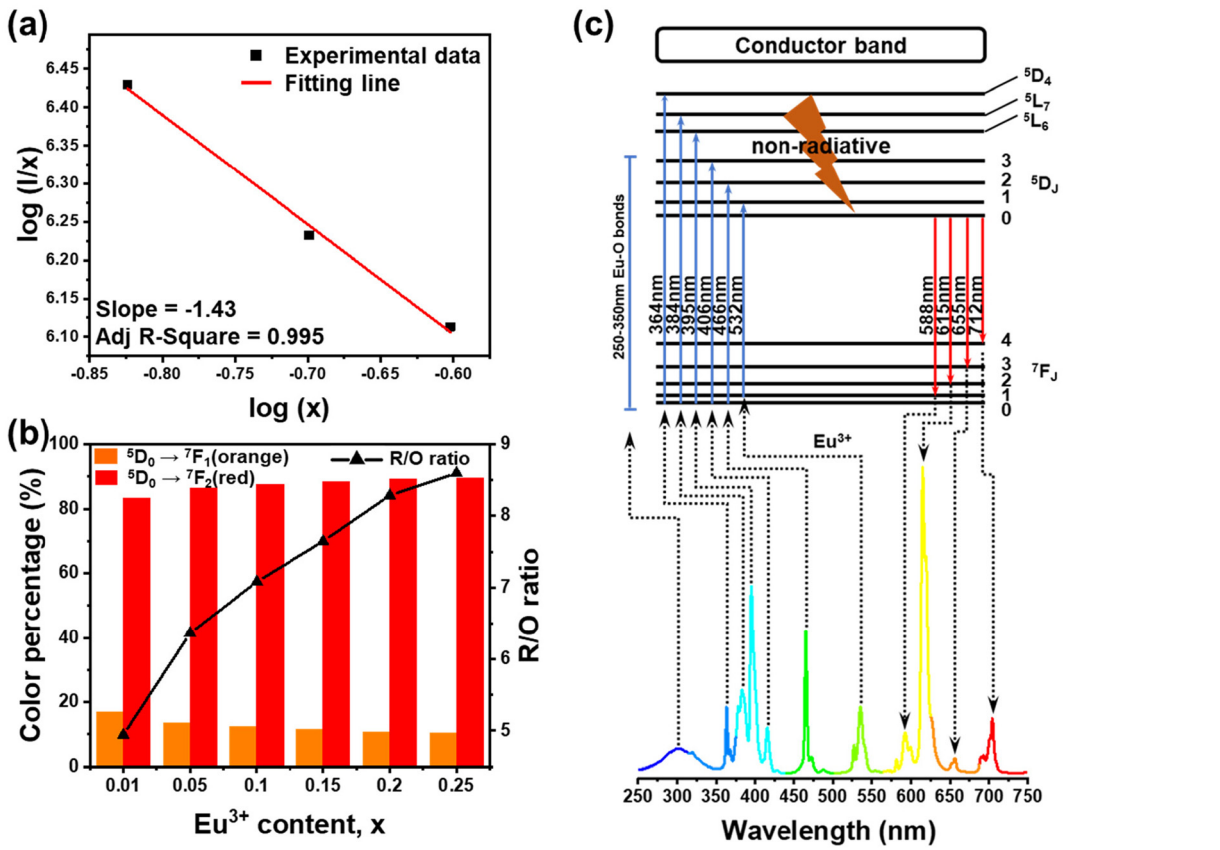

Fig. 6 (a) Log(I/x) *vs.* log(x) plot of the integrated emission intensity and linear fitting line for the $Ca_4Nb_2O_9$:xEu^{3+} phosphors, (b) red and orange color percentage and R/O ratio change with increasing the Eu^{3+} ion concentration in the $Ca_4Nb_2O_9$:xEu^{3+} phosphors, and (c) schematic energy level diagram of Eu^{3+} ions in $Ca_4Nb_2O_9$.

($^5D_0 \rightarrow {}^7F_1$) and ED transition ($^5D_0 \rightarrow {}^7F_2$) are provided in Fig. 6(b). As the Eu^{3+} ion concentration increased, the red-to-orange ratio (R/O) increased, which results from environment changes. Generally, the $^5D_0 \rightarrow {}^7F_2$ (orange) transition is an ultrasensitive ED transition highly sensitive to the crystal site environment. The $^5D_0 \rightarrow {}^7F_1$ (red) transition is an MD transition, which remains stable even when the crystal structure changes.[50,51] As the concentration of Eu^{3+} ions rises, they continuously occupy the sites of Ca^{2+}, destroying the symmetry of the structure and making the ratio shift towards $^5D_0 \rightarrow {}^7F_2$ transition.[52] This indicates that with the increase in Eu^{3+} ions, the color of $Ca_4Nb_2O_9:Eu^{3+}$ shifts towards the red side. Interestingly, the full width at half maximum (FWHM) of the $Ca_4Nb_2O_9:0.15Eu^{3+}$ phosphor was approximately 8 nm, which was much narrower than those of typical red-emitting phosphors used in displays such as $Sr_2Si_5N_8:Eu^{2+}$ (FWHM = 86 nm),

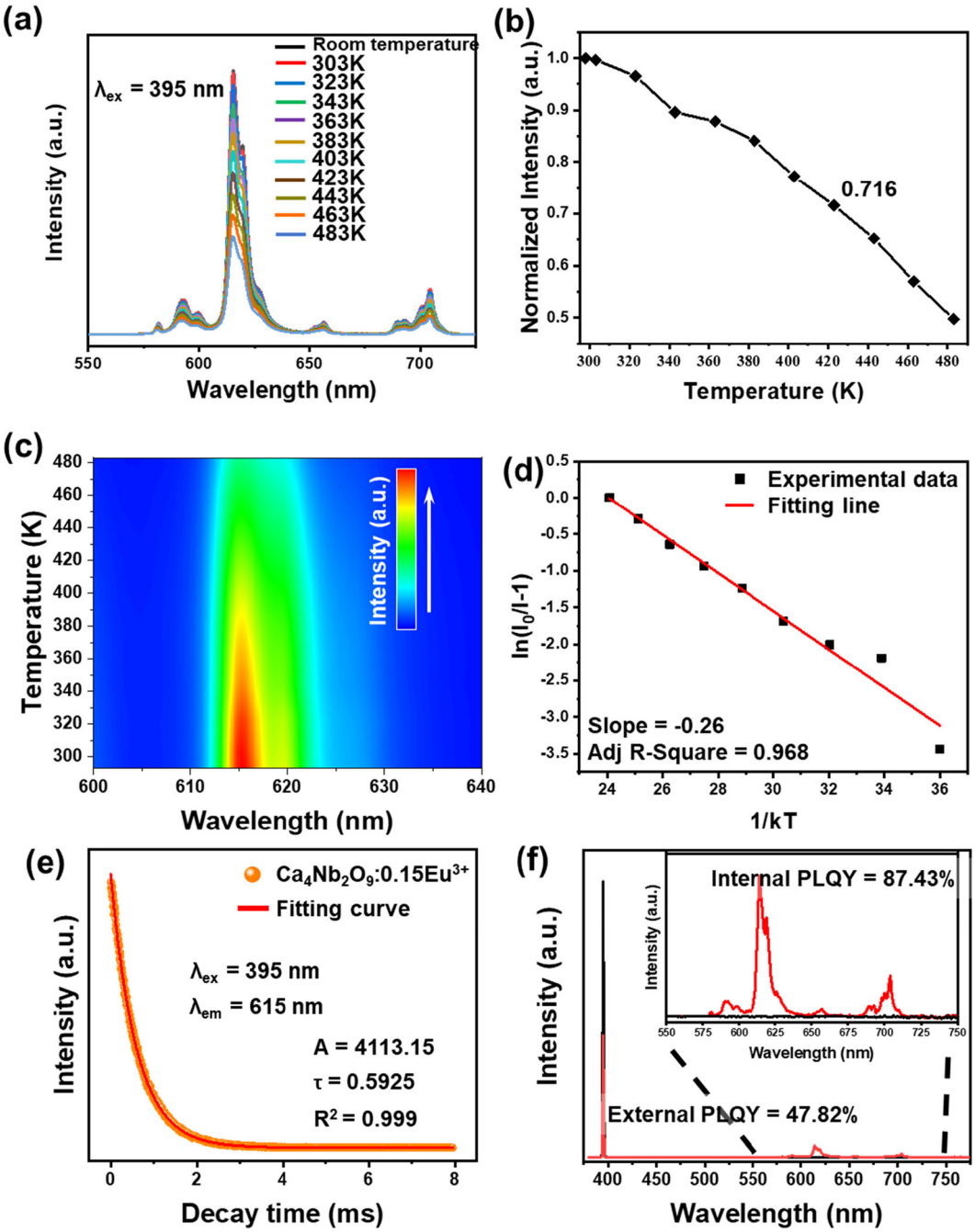

Fig. 7 (a) PL emission spectra of the $Ca_4Nb_2O_9:0.15Eu^{3+}$ phosphor under various temperature conditions. (b) Normalized emission intensity, (c) contour plot of main peak intensity as a function of temperature, (d) $\ln(I_0/I - 1)$ *vs.* $1/kT$ plot and linear fitting, (e) PL decay curve, and (f) PLQY values of the $Ca_4Nb_2O_9:0.15Eu^{3+}$ phosphor under excitation at 395 nm and emission at 615 nm.

$CaAlSiN_3:Eu^{2+}$ (FWHM = 94 nm), and KSF:Mn^{4+} (FWHM = 30 nm).[53–55] This performance is attributed to the hypersensitive $^5D_0 \rightarrow {}^7F_2$ transition.[56]

The luminescence spectrum in Fig. 6(c) illustrates the Eu^{3+} energy levels in the $Ca_4Nb_2O_9$ host, which is responsible for the excitation and emission processes. Electrons in the valence band are excited by higher energy radiation and transferred to the excited states. After progressing down to $^5D_0$ through NR transition, it finally descended to ^7F_J (where J = 0, 1, 2, 3, and 4) states, releasing the energy gap between the valence band and conduction band as photons.[57] The main absorption peak at 395 nm showed that the as-synthesized phosphor could be efficaciously excited by commercial UV LED chips.

To study the thermal stability, we measured the temperature-dependent PL spectra of the $Ca_4Nb_2O_9:0.15Eu^{3+}$ phosphor from room temperature towards 483 K, with the results presented in Fig. 7(a). The decrease in the intensity of the main peak can be clearly viewed in Fig. 7(b). However, the phosphor still had 71.6% intensity at a high temperature (423 K), indicating that the $Ca_4Nb_2O_9:0.15Eu^{3+}$ phosphor has good thermal stability. To better understand it, the contour plot of main peak intensity as a function of temperature is shown in Fig. 7(c). The Arrhenius equation, which is a typical formula for obtaining the activation energy (E_a), is given by:[58]

$$I_T = \frac{I_0}{1 + c\exp\left(\frac{-E_a}{kT}\right)} \quad (8)$$

where I_T and I_0 denote the intensities at temperatures T and 0 K, respectively, and c and k are constants. Through the linear fitting shown in Fig. 7(d), we obtained an activation energy of approximately 0.26 eV for the $Ca_4Nb_2O_9:0.15Eu^{3+}$ phosphor. The lifetime curves of the $Ca_4Nb_2O_9:0.15Eu^{3+}$ phosphor with an excitation wavelength of 395 nm, monitored at 615 nm, are shown in Fig. 7(e). The decay curve could be well-fitted using a single exponential equation:[15]

$$I = I_0 + A \times \exp\left(\frac{-t}{\tau}\right) \quad (9)$$

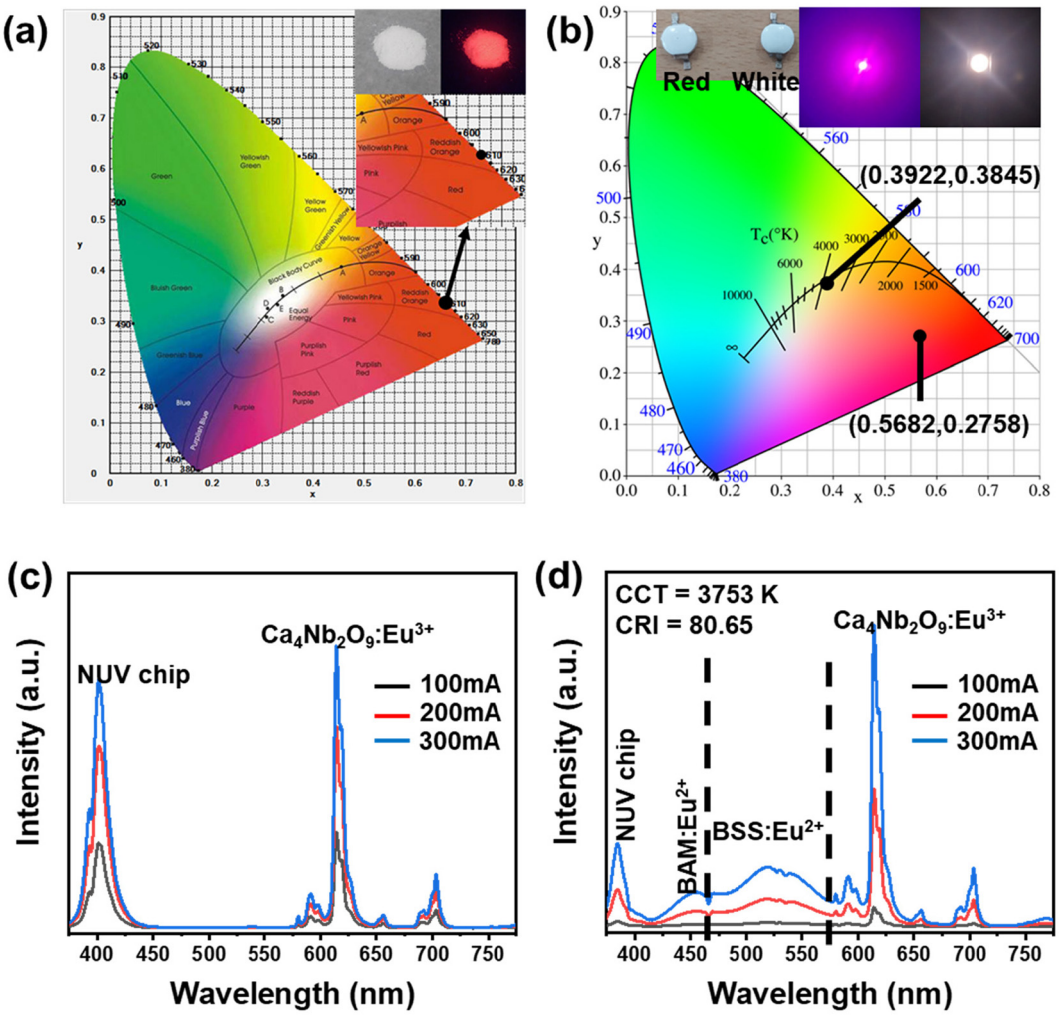

Fig. 8 (a) CIE chromaticity coordinates and photographic images of the resultant phosphor under room light and UV radiation for the $Ca_4Nb_2O_9:0.15Eu^{3+}$ phosphor. (b) CIE chromaticity coordinates and photographic images of the fabricated LED device under no bias and at a forward bias current of 100 mA. EL emission spectra of the packaged (c) red-emitting LED and (d) WLED devices at various driving currents.

where I and I_0 represent the luminescence intensities at times of $t = 0$ and t, respectively, A is a constant, and τ is the lifetime. In this experiment, τ was determined to be 0.5925 ms with an excellent adjusted R-square value of 0.999. The PLQY of the optimal sample $Ca_4Nb_2O_9$:0.15Eu^{3+} was obtained at the excitation wavelength of 395 nm and an emission wavelength of 615 nm. The following equations are introduced for internal and external PLQY:[59]

$$\text{Internal PLQY} = \frac{\int L_S}{\int E_R - \int E_S} = \frac{I_{em}}{I_{abs}} \quad (10)$$

$$\text{External PLQY} = \text{Internal PLQY} \times I_{abs} \quad (11)$$

where L_S is the emission spectrum, and E_R and E_S are the spectra of the excitation light with and without the sample, respectively. Therefore, the internal PLQY value of the $Ca_4Nb_2O_9$:0.15Eu^{3+} phosphor was calculated to be 87.43%, and I_{abs} was 0.547. The external PLQY value was determined to be 47.81% at an excitation wavelength of 395 nm, as shown in Fig. 7(f).

The CIE chromaticity coordinate (x, y) of the optimal sample with the excitation radiation of 395 nm and the photographs under normal light and 365 nm NUV light are shown in Fig. 8(a). At an excitation wavelength of 395 nm, the $Ca_4Nb_2O_9$:0.15Eu^{3+} phosphor exhibited the CIE chromaticity coordinate of (0.6629 and 0.3344). In addition, the following equation was used to evaluate the color purity for the red emission of the $Ca_4Nb_2O_9$:0.15Eu^{3+} phosphor under 395 nm excitation:[60]

$$\text{Color purity} = \sqrt{\frac{(x - x_i)^2 + (y - y_i)^2}{(x_d - x_i)^2 + (y_d - y_i)^2}} \quad (12)$$

where (x, y), (x_i, y_i), and (x_d, y_d) are the CIE chromaticity coordinates of the $Ca_4Nb_2O_9$:0.15Eu^{3+} phosphor, while the white illuminant point and dominant wavelength point are (0.310, 0.316) and (0.6801, 0.3197), respectively. Therefore, the color purity could be calculated as 95.5%, implying that the as-prepared phosphor is beneficial as a red light source in WLED applications. Additionally, the CIE chromaticity coordinates of the fabricated red and white LED devices and their photographic images under 100 mA of forward bias current are compared in Fig. 8(b). When the forward bias current was 100 mA, the CIE chromaticity coordinate of the red-emitting LED device was (0.5682, 0.2758), and for the WLED, it was (0.3922, 0.3845). Fig. 8(c) and (d) show the electroluminescence (EL) spectra of the fabricated red-emitting and white LED devices under different forward bias currents ranging from 100 to 300 mA. For the white LEDs, the correlated color temperature (CCT) reached 3753 K, indicating that the LED could supply outstanding warm light, and the color rendering index (CRI) was 80.65, which exceeded the threshold for lighting and display applications. Table 1 shows that the CRI and CCT of

Table 1 Comparative CRI and CCT of different phosphors

Compound	CRI	CCT (K)	Ref.
TeO_2-ZnO-B_2O_3-BaO	73.2	4920	61
$Ba_3La_6(SiO_4)_6$:Er^{3+}/Eu^{3+}	70.6	3946	62
$Sr_2NaMg_2V_3O_{12}$:Eu^{3+}	62	5100	63
$Ba_5Si_{11}Al_7N_{25}$:Eu^{2+}	63.6	3412	64
Sr_2YSbO_6:Mn^{4+}/Li^+	80.2	4487	65
$Ca_4Nb_2O_9$:Eu^{3+}	80.65	3753	This work

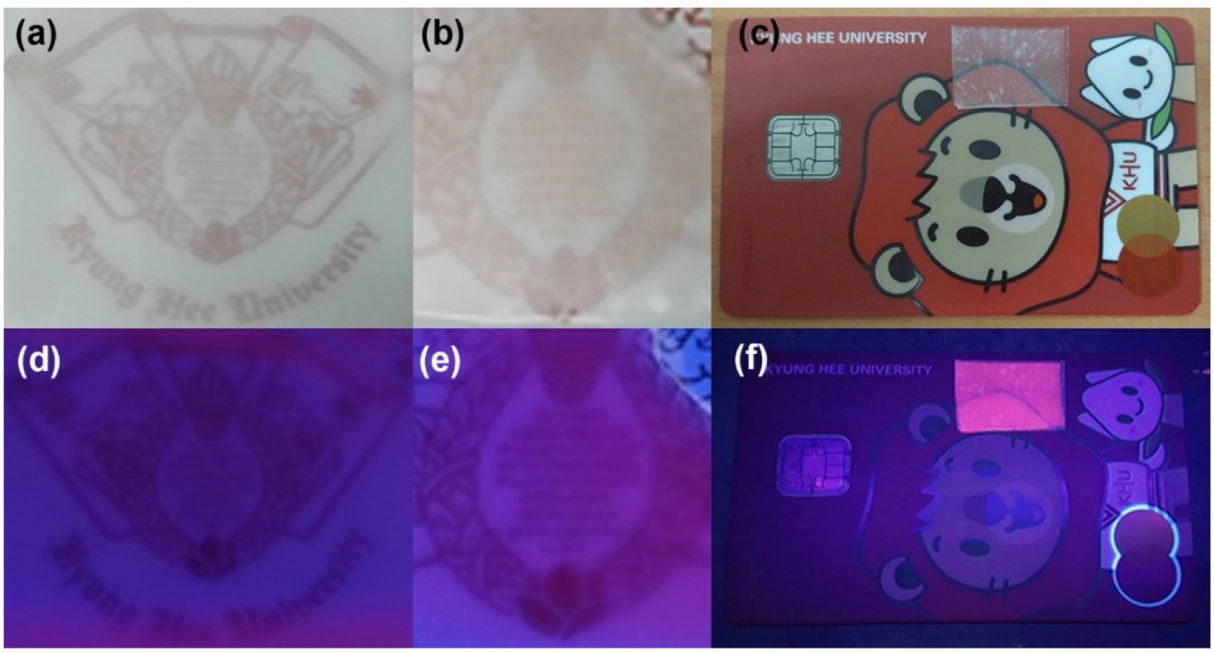

Fig. 9 Photographic images of the fabricated anti-counterfeiting film attached to plastic, glass, and card under room light (a–c) and 365 nm illumination (d–f).

$Ca_4Nb_2O_9:Eu^{3+}$ were better than those of many other phosphors, including the TeO_2-ZnO-B_2O_3-BaO, $Ba_3La_6(SiO_4)_6:Er^{3+}/Eu^{3+}$, $Sr_2NaMg_2V_3O_{12}:Eu^{3+}$, $Ba_5Si_{11}Al_7N_{25}:Eu^{2+}$, and $Sr_2YSbO_6:Mn^{4+}/Li^+$.[61–65] Therefore, the $Ca_4Nb_2O_9:Eu^{3+}$ phosphor with excellent optical properties was determined to be a feasible red phosphor suitable for WLEDs.

These outstanding properties make the $Ca_4Nb_2O_9:Eu^{3+}$ phosphor suitable for anti-counterfeiting applications. In this study, the phosphor was incorporated into a PVA solution for anti-counterfeiting films. To investigate its versatility, the films were applied to plastic, glass, and the Kyung Hee University student card, as shown in Fig. 9(a–c), respectively. The films appeared white and translucent under daylight irradiation, allowing the covered information to be fully visible. However, when exposed to UV radiation (365 nm), the patterns emitted bright red light, making them easily discernible. These results suggest that the Eu^{3+}-activated $Ca_4Nb_2O_9$ phosphors are prospective candidates for optical anti-counterfeiting films on various substrates.

4. Conclusion

A series of advanced high-purity red-emitting $Ca_4Nb_2O_9:Eu^{3+}$ phosphors were synthesized using a high-temperature solid-state method. XRD, XPS, FE-SEM, and EDS analyses were performed to investigate the structural properties. The PL properties reached their maximum when the Eu^{3+} ion concentration was 15 mol%, and the electric d–d interaction was confirmed to be the main reaction in the concentration quenching mechanism. The temperature stability of this phosphor was good, as it remained at 71.6% when the temperature was increased to 423 K (which is generally considered to be the working temperature of LEDs). Moreover, no shift in PL emission peaks was observed. The $Ca_4Nb_2O_9:0.15Eu^{3+}$phosphor had a CIE chromaticity coordinate of (0.6629, 0.3344) with a color purity of 95.5%. Combining the resultant phosphor with commercial blue and green phosphors enabled the fabrication of a warm-light white LED device with CCT of 3753 K and CRI of 80.65. From these results, the proposed red-emitting $Ca_4Nb_2O_9:Eu^{3+}$ phosphors are potential candidates for solid-state lighting applications based on WLED. Furthermore, the applicability of the resultant phosphors to optical security films was verified.

Conflicts of interest

There are no conflicts to declare.

Acknowledgements

This work was supported by the National Research Foundation of Korea (NRF) grant funded by the Korea government (MSIP) (No. RS-2023-00252268).

References

1 G. Wu, J. Xue, X. Li, Q. Bi, M. Sheng and Z. Leng, *Ceram. Int.*, 2023, **49**, 10615–10624.
2 N. K. Mishra, A. Kumar and K. Kumar, *J. Alloys Compd.*, 2023, **947**, 169440.
3 X. Hu, A. Zhang, H. Sun, F. Zeng, Y. Lei, L. Xie, R. Yu, B. Deng and H. Lin, *J. Lumin.*, 2023, **258**, 119806.
4 S. Wu, Q. Liu, M. G. Brik, P. Xiong, D. Wang, G. Zhang and Y. Chen, *J. Am. Ceram. Soc.*, 2022, **105**, 5793–5806.
5 H. Fan, Z. Lu, Y. Meng, P. Chen, L. Zhou, J. Zhao and X. He, *Opt. Laser Technol.*, 2022, **148**, 017804.
6 X. Li, S. Chen, K. Zhang, S. Deng, J. He, B. Wang and Q. Zeng, *Mater. Today Chem.*, 2023, **30**, 101594.
7 Y. Hua, T. Wang, H. Li, J. S. Yu and L. Li, *J. Alloys Compd.*, 2023, **930**, 167454.
8 C. M. Nandanwar, N. S. Kokode, A. N. Yerpude and S. J. Dhoble, *Mater. Lett.: X*, 2023, **18**, 100202.
9 M. Ibrahim, M. Iqbal, Y.-T. Tang, S. Khan, D.-X. Guan and G. Li, *Agronomy*, 2022, **12**, 2539.
10 Y. Tang, X. He, Y. Zhang, H. Yuan, Y. Xin, X. Ren, Q. Chen and H. Yin, *J. Alloys Compd.*, 2022, **899**, 163347.
11 I. H. Cho, G. Anoop, D. W. Suh, S. J. Lee and J. S. Yoo, *Opt. Mater. Express*, 2012, **2**, 1292–1305.
12 Y. Gao, R. Iwasaki, D. Hamana, J. Iihama, S. Honda, M. Kumari, T. Hayakawa, S. Bernard, P. Thomas and Y. Iwamoto, *Int. J. Appl. Ceram. Technol.*, 2023, **20**, 153–165.
13 W. C. Lee, H. K. Yang, M. Kwak and B. K. Moon, *Optik*, 2018, **172**, 1205–1210.
14 H. Ruan, T. Wang, L. Wang, Y. Li, J. Lei, D. Deng, J. Qiang, S. Liao and Y. Huang, *Ceram. Int.*, 2023, **49**, 35165–35174.
15 S. Lai, M. Zhao, Y. Zhao, M. S. Molokeev and Z. Xia, *ACS Mater. Au*, 2022, **2**, 374–380.
16 Z. Liu, Z. Li, T. Seto and Y. Wang, *Adv. Opt. Mater.*, 2023, **11**, 2300845.
17 P. Sharma, J. Madda and S. Vaidyanathan, *Dalton Trans.*, 2023, **41**, 15043–15056.
18 P. Linghu, X. Gong, J. Zhang, R. Cui and X. Guo, *J. Solid State Chem.*, 2023, **327**, 124282.
19 M. Rajendran and S. Vaidyanathan, *ChemistrySelect*, 2020, **5**, 5128–5136.
20 J. K. Lee, Y. Hua and J. S. Yu, *Ceram. Int.*, 2024, **50**, 484–494.
21 G. Yuan, R. Cui, J. Zhang, X. Qi and C. Deng, *Optik*, 2021, **232**, 166513.
22 Q. Chen, X. Guo, J. Zhang, H. Xu, M. Hu and R. Cui, *J. Lumin.*, 2023, **258**, 119812.
23 X. Hu, A. Zhang, R. Tang, X. Jin, J. Che, X. Ouyang, C. Zhou, L. Xie, B. Deng and R. Yu, *J. Alloys Compd.*, 2023, **938**, 168540.
24 R. Cao, H. Xiao, F. Zhang, Z. Luo, T. Chen, W. Li, P. Liu and G. Zheng, *J. Lumin.*, 2019, **208**, 350–355.
25 P. Du, X. Sun, Q. Zhu and J.-G. Li, *Scr. Mater.*, 2020, **185**, 140–145.
26 H. Zhang, Z. Gao, G. Li, Y. Zhu, S. Liu, K. Li and Y. Liang, *Chem. Eng. J.*, 2020, **380**, 122491.

27 P. Zhang, N. Li, Z. Wei, Z. Wang, M. Gou, L. Zhao, W. Chen and Q. Qiang, *New J. Chem.*, 2021, **45**, 66–75.
28 R. Mi, Y. Liu, L. Mei, X. Min, M. Fang, X. Wu, Z. Huang and C. Chen, *Chem. Eng. J.*, 2023, **457**, 141377.
29 X. Yu, H. Zhang and J. Yu, *Aggregate*, 2021, **2**, 20–34.
30 B. Verma, R. N. Baghel, D. P. Bisen, N. Brahme and V. Jena, *Opt. Mater.*, 2022, **123**, 111787.
31 H. Fan, X. Meng, Y. Xu, Y. Lu and Y. Liu, *Opt. Mater.*, 2023, **140**, 113871.
32 R. Song, H. Tang, J. Li, Y. Niu, Y. Liu, J. He and J. Zhu, *Opt. Mater.*, 2024, **148**, 114859.
33 M. Deng, S. Huang, Y. Sun, Y. Wang, Y. Yan and M. Shang, *J. Lumin.*, 2023, **263**, 120137.
34 R. Bian, S. An, X. Wang, Y. Xue, J. Tian, Z. Liang and Z. Song, *Int. J. Hydrogen Energy*, 2024, **51**, 787–795.
35 Z. Liu, Y. Huang, T. Chen and W. Feng, *J. Solid State Chem.*, 2024, **329**, 124431.
36 J. Y. Choi, J. M. Lee, Y. K. Baek, J. G. Lee and Y. K. Kim, *Dalton Trans.*, 2021, **50**, 14560–14565.
37 Y. Qiu, R. Cui, J. Zhang and C. Deng, *J. Solid State Chem.*, 2023, **327**, 124265.
38 G. R. Mamatha, B. R. R. Krushna, J. Malleshappa, B. Subramanian, B. D. Prasad, C. Srikanth and H. Nagabhushana, *J. Photochem. Photobiol., A*, 2023, **439**, 114560.
39 A. Shaukat, M. A. Farrukh, K.-K. Chong, R. Nawaz, M. T. Qamar, S. Iqbal, N. S. Awwad and H. A. Ibrahium, *Catalysts*, 2023, **13**, 1135.
40 S. Kumari, A. S. Rao and R. K. Sinha, *J. Mol. Struct.*, 2024, **1295**, 136507.
41 Z. Guo, H. Jiang, H. Li, H. Zhang, C. Liu, R. Zhao, Z. Yang, H. Tang, J. Li, J. Zhang and J. Zhu, *Appl. Mater. Today*, 2024, **37**, 102095.
42 X. Han, C. Xin, S. Wang, J. Wu, Z. Ye, H. Yu and H. Zhang, *Inorg. Chem.*, 2023, **62**, 9679–9686.
43 N. Shaishta, W. U. Khan, S. K. B. Mane, A. Hayat, D.-D. Zhou, J. Khan, N. Mehmood, H. K. Inamdar and G. Manjunatha, *Int. J. Energy Res.*, 2020, **44**, 8328–8339.
44 J. Xu, J. Luo, L. Zeng, Y. Tao, G. Li, C. Li, J. Liu, L. Zhou, S. Hu, J. Yang, F. Lin and J. Tang, *Ceram. Int.*, 2023, **49**, 17271–17282.
45 Q. Wu, Y. Li, Y. Wang, H. Liu, S. Ye, L. Zhao, J. Ding and J. Zhou, *Chem. Eng. J.*, 2020, **401**, 126130.
46 J. Du, S. Liu, Z. Song and Q. Liu, *ACS Appl. Mater. Interfaces*, 2023, **15**, 53738–53745.
47 G. Lu, Y. Wang, S. Piao, J. Zhang, X. Zhang, X. Zhou, Y. Cao, X. Li and B. Chen, *J. Am. Ceram. Soc.*, 2023, **106**, 1216–1229.
48 A. Bashiri, A. Vaskin, K. Tanaka, M. Steinert, T. Pertsch and I. Staude, *ACS Nano*, 2024, **18**, 506–514.
49 F. Xie, J. Gu, S. Zhong, P. Zhang, Y. Wen, Y. Li, H. Xu, S. Yao, Q. Zhang and J. Li, *Mater. Today Chem.*, 2024, **37**, 102019.
50 A. Princy, E. A. Rathnakumari and S. M. M. Kennedy, *J. Am. Ceram. Soc.*, 2023, **106**, 5364–5380.
51 J. L. B. Martin, M. F. Reid and J.-P. R. Wells, *J. Alloys Compd.*, 2023, **937**, 168394.
52 Y. Jin, Z. Zhou, R. Ran, S. Tan, Y. Liu, J. Zheng, G. Xiang, L. Ma and X.-J. Wang, *Adv. Opt. Mater.*, 2022, **10**, 2202049.
53 L. I. U. Chang, Z. Bi, H. A. O. Lüyuan and X. U. Xin, *J. Rare Earths*, 2014, **32**, 691–695.
54 Y. Shen, W. Zhuang, Y. Liu, H. He and T. He, *J. Rare Earths*, 2010, **28**, 289–291.
55 H. Tian, T. Seto and Y. Wang, *Small Methods*, 2023, **7**, 2300305.
56 A. M. Voiculescu, S. Hau, G. Stanciu and C. Gheorghe, *J. Alloys Compd.*, 2023, **958**, 170507.
57 C. Wang, R. Cui, J. Zhang, Y. Tai, T. Zhao, B. Zhang and C. Deng, *Opt. Mater.*, 2023, **140**, 113891.
58 Z. Yang, Y. Zhao, Y. Zhou, J. Qiao, Y.-C. Chuang, M. S. Molokeev and Z. Xia, *Adv. Funct. Mater.*, 2022, **32**, 2103927.
59 Y. Li, Y. Yin, T. Wang, J. Wu, J. Zhang, S. Yu, M. Zhang, L. Zhao and W. Wang, *Dalton Trans.*, 2021, **50**, 4159–4166.
60 S. Huang, L. Yu, K. Peng, Y. Zhao, J. Wang and M. Shang, *J. Am. Ceram. Soc.*, 2021, **104**, 5848–5858.
61 H. Li, P. Wang, Y. Zhuo, X. Cao and D. Xiong, *J. Am. Ceram. Soc.*, 2020, **103**, 5056–5066.
62 H. Patnam, S. K. Hussain and J. S. Yu, *J. Lumin.*, 2020, **223**, 117204.
63 J. Li, B. Liu, G. Liu, Q. Che, Y. Lu and Z. Liu, *J. Rare Earths*, 2023, **41**, 1689–1695.
64 C. He, T. Takeda, Z. Huang, J. Xu, J. Chen, W. Yi, R. Xie and N. Hirosaki, *Chem. Eng. J.*, 2023, **455**, 140932.
65 G. Li, X. Lu, Q. Mao, G. Du, M. Liu, L. Chu and J. Zhong, *Mater. Today Chem.*, 2022, **23**, 100744.